Romanian Reports in Physics, Vol. 68, No. 4, P. 1447–1465, 2016

STUDY OF ELECTRON CAPTURE RATES ON CHROMIUM ISOTOPES FOR CORE-COLLAPSE SIMULATIONS

MUHAMMAD MAJID AND JAMEEL-UN NABI

Faculty of Engineering Sciences,
GIK Institute of Engineering Sciences and Technology, Topi 23640, Khyber Pakhtunkhwa, Pakistan
Email: *majid.phys@gmail.com, jameel@giki.edu.pk*

Received December 29, 2015

Abstract. Electron capture rates on *fp*-shell nuclei play a pivotal role in the dynamics of stellar evolution and core collapse. These rates play a crucial role in the gravitational collapse of the core of a massive star activating the supernova explosion. As per simulation results, capture rates on chromium isotopes have a major impact on controlling the lepton-to-baryon fraction of the stellar core during the late phases of evolution of massive stars. In this paper we calculate the electron capture rates on isotopes of chromium with mass range $42 \leq A \leq 65$, including neutron-deficient and neutron-rich isotopes. For the calculation of weak rates in stellar matter, we used the pn-QRPA model with separable Gamow-Teller forces and took deformation of nucleus into consideration. A recent study proved this form of pn-QRPA to be the best for calculation of GT strength distributions amongst the pn-QRPA models. The stellar weak rates are calculated over a broad range of temperature $(0.01 \times 10^9 - 30 \times 10^9 (K))$ and density $(10 - 10^{11} (g/cm^3))$ domain. We compare our electron capture rates with the pioneering calculation of Fuller, Fowler, and Newman (FFN) and with the large-scale shell model (LSSM) calculation. Our electron capture rates are enhanced compared to the FFN and shell model rates.

Key words: Gamow-Teller transitions; electron capture rates; positron decay rates; pn-QRPA theory; stellar evolution; core-collapse; Ikeda sum rule.

PACS: 23.40.Bw, 23.40.-s, 26.30.Jk, 26.50.+x, 97.10.Cv

1. INTRODUCTION

The Gamow-Teller ($GT_{\pm}$) transitions are the most useful nuclear weak decay processes of the spin-isospin ($\sigma\tau_{\pm}$) type. These transitions are not only important in nuclear physics, but also in astrophysics where they play a decisive role in nucleosynthesis and in supernova explosions [1]. The weak interactions strongly effect the late evolution phases of massive stars. Their operation controls the ratio of electron to baryon (Y_e) content of stellar matter and core entropy of the presupernova star and thus its Chandrasekhar mass that is proportional to ${Y_e}^2$ [2]. The electron capture decreases the number of available electrons for pressure support, whereas β-decay proceeds in the reverse direction. (Anti)neutrinos are produced in both processes,

and escape from the stars having densities less than 10^{11} g/cm^3 thereby carrying out entropy and energy away from the core. The β-decay and electron capture rates are dominated by Fermi and GT transitions. Whereas the behavior of Fermi transitions (only significant in β-decays) is simple, an accurate description of GT strength is a complex problem. Nuclei are completely ionized in the stellar environment and as a result continuum electron capture from the degenerate electron plasma occurs. The electron energies are high enough to persuade transitions to GT resonance. The β-decay and electron capture happen during the time of hydrostatic burning phases. Furthermore, during final astrophysical evolutionary phases, the importance of these processes increases when the temperature and density of the core become huge and the rising Fermi energy of the electrons makes the capture favorable [3].

For *fp*-shell nuclides the GT transitions are considered extremely essential for supernova physics [3, 4]. GT transitions in chromium isotopes have a special mention as per simulation results of presupernova evolution of massive stars (e.g. [5, 6]). Not many measurements of GT strength in chromium isotopes have been carried out to the best of our knowledge. Zioni *et al.* (1972) first studied the decay of ^{46}Cr, by using the ^{32}S(^{16}O, 2n) reaction to create ^{46}Cr [7]. Onishi and collaborators (2005) examined the beta decay of ^{46}Cr to the 1^+ states at 993 keV excitation energy in ^{46}V. The T=1 nucleus decays to T=0 and 1^+ levels of daughter nucleus, termed as favored-allowed GT transitions having small *ft*-value. This experiment was done at RIKEN accelerator research facility. Fujita *et al.* (2011) performed a ^{50}Cr(^{3}He,t)^{50}Mn reaction experiment and made measurements up to 5 MeV in daughter nuclei [8]. But it was Adachi and collaborators (2007) who performed a high resolution ^{50}Cr(^{3}He,t)^{50}Mn measurement at 0° and at incident energies of 140 MeV per nucleon in order to study GT transitions precisely. In this experiment the authors measured GT strength up to 12 MeV in ^{50}Mn [9].

There is a need to obtain more experimental data on GT strength in *fp*-shell nuclei. Next-generation radioactive ion-beam facilities (e.g. FAIR (Germany), FRIB (USA) and FRIB (Japan)) are expected to provide us measured GT strength distributions of many more nuclei. It is also important to examine the GT strength in exotic nuclide close to proton and neutron drip lines. Simulation of stellar events require GT strength distributions, preferably for hundreds of nuclei. Because of scarcity of experimental data, one is compelled to calculate GT strength distributions for *fp*-shell nuclei using a microscopic nuclear model [10]. It is also essential to note that in the *fp*-shell nuclides, the GT strength is distributed over several discrete states (i.e. strength is fragmented) and in presupernova models the information of these low-lying strengths is very significant for a precise time evolution of Y_e [3, 5]. The knowledge of measured GT strength should be broadened and theoretical attempts should be done to reproduce them and calculate strengths of nuclei far from line of stability [11, 12].

The first extensive attempt for the calculation of weak rates at high densities and temperatures was performed by Fuller, Fowler, and Newman (FFN) [3]. FFN estimated these weak rates over a wide density and temperature range i.e. $10 \leq \rho Y_e$(g cm^3)$\leq 10^{11}$, $10^7 \leq$T(K)$\leq 10^{11}$. The excitation energies and GT strengths were calculated by employing a zeroth-order shell model. The experimental results available at that time were also incorporated. The FFN work for *fp*-shell nuclei was later extended by [5]. We present here the microscopic calculation of GT strength distributions and electron capture rates for 24 chromium isotopes (^{42}Cr - ^{65}Cr) using the proton-neutron quasiparticle random phase approximation (pn-QRPA) model. This model [13–15] is proven to be a very good microscopic model for the β-decay half-life estimations far from the stability [15, 16]. The pn-QRPA theory was also effectively used in the past for the calculation of EC/β^+ half lives and was found to be in excellent comparison with the experimental half-lives [17]. The pn-QRPA model was later modified to treat nuclear excited state transitions [18]. In view of successfully calculating the terrestrial decay rates, Nabi and Klapdor-Kleingrothaus, for the first time, used this theory to calculate the stellar weak rates and energy losses in stellar matter for sd- [19] and fp/fpg-shell nuclei [20]. Reliability of the calculated stellar weak rates using the pn-QRPA model was discussed in detail in Ref. [20]. There the authors compared the pn-QRPA calculations with measured data for thousands of nuclei and obtained satisfactory results (see also [21]). A recent study took six different pn-QRPA models to study the GT strength distributions in chromium isotopes [4]. The authors concluded that the current pn-QRPA model was the best amongst all the other pn-QRPA models and reproduced well the available experimental data and also possessed the best predictive power for estimation of half-lives for unknown nuclei. Another benefit of using the pn-QRPA theory is that large configuration spaces can be handled, which are not possible in shell model calculations. Consequently we decided to use the same model (along with same model parameters) to calculate stellar electron capture rates on isotopes of chromium.

The theoretical formalism used for the calculation of electron capture rates is briefly discussed in next section. In Sect. 3 the calculated weak rates are presented and also compared with previous calculations. Finally the conclusions are drawn in Sect. 4.

2. THEORETICAL FORMALISM

The formalism used to determine the GT strength and stellar electron capture rates using the pn-QRPA theory is reviewed in this section. We made the following assumptions in the calculations.

(i) Only super-allowed Fermi and GT transitions were calculated. The contri-

butions from forbidden transitions were presumed relatively negligible.

(ii) The temperature was assumed high enough so that the electrons were not bound to the nucleus anymore and obeyed the Fermi-Dirac distribution. At kT $>$ 1 MeV, positrons come out via electron-positron pair creation, and take the same energy distribution function as the electrons.

(iii) The distortion of electron wave function due to the Coulomb interaction with nucleus was represented by the Fermi function in the phase space integrals.

(iv) Neutrinos and antineutrinos escaped freely from the stellar interior, and their captures were not considered.

To start our calculations the Hamiltonian was chosen as

$$H^{QRPA} = H^{sp} + V^{pair} + V^{ph}_{GT} + V^{pp}_{GT}, \tag{1}$$

where H^{sp} represents the single-particle Hamiltonian, V^{pair} denotes the pairing force, V^{ph}_{GT} represents the particle-hole (ph) GT force and V^{pp}_{GT} is the particle particle (pp) GT force. Single particle energies and wave functions were calculated in the Nilsson model [22], in which the nuclear deformations was considered. Pairing among nucleons was incorporated within the BCS approximation. The proton-neutron residual interactions appear in two different forms, i.e. ph and pp interactions, characterized by two interaction constants χ and κ, respectively. The selections of these two constants were done in an optimal fashion to reproduce available experimental data and fulfilment of model independent Ikeda sum rule [23]. In this paper, we chose the value of χ to be 4.2/A, showing a $1/A$ dependence [24] and κ equal to 0.10. Other parameters necessary for electron capture calculations are the nuclear deformations, Nilsson potential parameters, the pairing gaps, and the Q-values. Nilsson-potential parameters were chosen from [25] and the Nilsson oscillator constant was taken as $\hbar\omega = 41A^{-1/3}$ (MeV), the same for neutrons and protons. The computed half-lives depend just weakly on the pairing gaps values [26]. Therefore, the conventional values of

$$\Delta_p = \Delta_n = 12/\sqrt{A}\,(\mathrm{MeV})$$

were applied in this work. Experimentally adopted values of the deformation parameters, for even-even isotopes of chromium (^{48,50,52,54}Cr), extracted by relating the measured energy of the first 2^+ excited state with the quadrupole deformation, were taken from [27]. For other cases the deformation of the nucleus was calculated as

$$\delta = \frac{125(Q_2)}{1.44(Z)(A)^{2/3}}, \tag{2}$$

where Z and A are the atomic and mass numbers, respectively, and Q_2 is the electric quadrupole moment taken from Möller and Nix [28]. Q-values were taken from the recent mass compilation of Audi and collaborators [29].

The electron capture (EC) and positron decay (PD) rates from the parent nucleus *i*-th state to the daughter nucleus *j*-th state is specified by

$$\lambda_{ij}^{EC(PD)} = \ln 2 \frac{f_{ij}^{EC(PD)}(T, \rho, E_f)}{(ft)_{ij}} \tag{3}$$

where $(ft)_{ij}$ is connected to the reduced transition probability (B_{ij}) by

$$(ft)_{ij} = D/B_{ij} \tag{4}$$

where D is constant and is given as

$$D = \frac{2 \ln 2 \hbar^7 \pi^3}{g_v^2 m_e^5 c^4} \tag{5}$$

and B_{ij} is given by

$$B_{ij} = B(F)_{ij} + ((g_A/g_V)^2 B(GT)_{ij} \tag{6}$$

We took the value of D = 6295 s [17] and g_A/g_V as -1.254. The reduced transition probabilities B(F) and B(GT) are specified by

$$B(F)_{ij} = \frac{1}{2J_i + 1} \langle j \parallel \sum_k t_{\pm}^k \parallel i \rangle|^2 \tag{7}$$

$$B(GT)_{ij} = \frac{1}{2J_i + 1} \langle j \parallel \sum_k t_{\pm}^k \overrightarrow{\sigma}^k \parallel i \rangle|^2 \tag{8}$$

here $\overrightarrow{\sigma}(k)$ is the spin operator and $t_{\pm}^k$ represent the isospin raising and lowering operator. For construction of parent and daughter excited states and calculation of nuclear matrix elements we refer to [19]. The phase space integral f_{ij} is an integral over total energy. For electron capture it is given by

$$f_{ij}^{EC} = \int_{w_l}^{\infty} w\sqrt{w^2 - 1}(w_m + w)^2 F(+Z, w) G_- dw, \tag{9}$$

and for positron emission

$$f_{ij}^{PD} = \int_1^{w_m} w\sqrt{w^2 - 1}(w_m - w)^2 F(-Z, w)(1 - G_+) dw. \tag{10}$$

Here w represents the total energy of the electron including its rest mass, and w_l denotes the total capture threshold energy (rest + kinetic) for electron capture. $G_-(G_+)$ is the electron (positron) distribution functions.

$$G_- = \left[\exp\left(\frac{E - E_f}{kT}\right) + 1\right]^{-1} \tag{11}$$

$$G_+ = \left[\exp\left(\frac{E + 2 + E_f}{kT}\right) + 1\right]^{-1} \tag{12}$$

Here $E = (w-1)$ is the kinetic energy of the electrons, E_f is the Fermi energy of the electrons, T is the temperature, and k is the Boltzmann constant. The Fermi functions $F(Z,w)$ are determined according to the procedure used by [30]. If the corresponding electron or positron emission total energy (w_m) is greater than -1, then $w_l = 1$, and if less than or equal to 1, then $w_l = |w_m|$, where w_m is the total β decay energy,

$$w_m = m_p - m_d + E_i - E_j \tag{13}$$

where m_p (m_d) and E_i (E_j) are mass and excitation energies of the parent (daughter) nucleus respectively. The number density of electrons linked with protons and nuclei is $\rho Y_e N_A$ (where ρ is the baryon density and N_A is Avogadro number)

$$\rho Y_e = \frac{1}{\pi^2 N_A}(\frac{m_e c}{\hbar})^3 \int_0^\infty (G_- - G_+) p^2 dp \tag{14}$$

where $p = (w^2-1)^{1/2}$ is the momentum of electron. Eq. 14 was used for an iterative calculation of Fermi energies for selected values of T and Y_e. As the temperature in the interior of stars is very high so there is a finite probability of occupation of parent excited states. The total EC and PD rates per unit time per nucleus is

$$\lambda^{EC(PD)} = \sum_{ij} P_i \lambda_{ij}^{EC(PD)}, \tag{15}$$

where P_i follows the normal Boltzmann distribution. In Eq. 15, the summation was taken over all the initial and final states until reasonable convergence was achieved in our calculated rates. The Fermi strength is concentrated in a very narrow resonance centered around the isobaric analogue state (IAS) for the ground and excited states. In case of Fermi strength the isobaric analogue state (IAS) was calculated by operating on the associated parent states with the isospin raising or lowering operator

$$T_\pm = \sum_i t_\pm(i),$$

where the sum runs over the nucleons. The Fermi matrix element depends only on the nuclear isospin (T) and its projection T_z (equal to (Z-N)/2) for the parent and daughter nucleus. The energy of the IAS was calculated according to [31] and the reduced transition probability was calculated using

$$B(F) = T(T+1) - T_{zi} T_{zf},$$

where T_{zi} and T_{zf} are the third components of the isospin of initial and final analogue states, correspondingly.

3. RESULTS AND DISCUSSION

Earlier in Ref. [4] three different QRPA models, namely the Pyatov method (PM), the Schematic model (SM) and the pn-QRPA model, were considered for the calculation of GT transitions in chromium isotopes. The idea was to study the GT transitions in different QRPA models. These models mainly studied the effect of deformation, particle-hole and particle-particle interactions in QRPA calculations. It was observed that the lowest total GT strength values were calculated by the PM. Further the PM model failed to yield the desired fragmented GT strength distribution. The reason was that the PM considered only spherical nuclei, due to which most of the GT strength was concentrated in one specific state. The biggest values of total GT strength was calculated by the SM, but it placed the GT centroid at much higher excitation energy in daughter nucleus. The PM also resulted in higher placement of centroid values in the daughter nuclei. On the other hand, the pn-QRPA model placed the centroids at lower energies in daughter which translated into stronger weak rates in astrophysical environment. Further it was shown that the pn-QRPA model compared well with measured GT strength distributions wherever available and emerged as the best model for calculation of GT strength distributions [4]. In this manuscript we use the same pn-QRPA model for the calculation of β-decay half-lives and stellar electron capture (EC) rates. We consider 24 isotopes of chromium, in mass range $^{42-65}$Cr, for the calculation of EC rates. These nuclei include both stable (^{50}Cr, $^{52-54}$Cr) and unstable isotopes of chromium, including neutron deficient and neutron rich cases. We quenched our pn-QRPA results by a factor of f_q^2 = $(0.6)^2$ [32, 33] in calculation of EC rates (akin to other microscopic calculations including shell model calculations). Interestingly [32] and [34] predicted the same quenching factor of 0.6 for the RPA calculation in the case of ^{54}Fe when comparing their measured strengths to RPA calculations.

Figure 1 shows that our calculated β-decay half-lives for isotopes of chromium agree quite well with the measured values. The experimental half-lives were taken from [29]. As mentioned earlier, ^{50}Cr, ^{52}Cr, ^{53}Cr and ^{54}Cr are stable isotopes of chromium.

The total GT$_+$ and GT$_-$ strengths (represented as $\sum$B(GT$_+$) and $\sum$B(GT$_-$) respectively, in this work) are related to the re-normalized Ikeda sum rule (ISR$_{re-norm}$) as

$$ISR_{re-norm} = \sum B(GT_-) - \sum B(GT_+) \cong 3f_q^2(N-Z). \qquad (16)$$

where *Z* and *N* represent the numbers of protons and neutrons, respectively [23]. Figure 2 shows the comparison of calculated $ISR_{re-norm}$ with the model-independent theoretical predictions. It is clear from Fig. 2 that the $ISR_{re-norm}$ is satisfied well by the pn-QRPA model (deviates at the maximum by only a few percent). The SM and PM models satisfied the Ikeda Sum Rule (ISR) for even-even Cr isotopes but

showed some deviations for odd-A cases. The pn-QRPA model fulfilled the ISR for both even-even and odd-A Cr isotopes.

The pn-QRPA calculated EC rates are shown in Table 1. We present these EC rates for temperatures (1, 3, 10 and 30)$\times 10^9 K$ and at selected densities (10^3, 10^7 and $10^{11} gcm^{-3}$). It is to be noted that the calculated EC rates (Eq. 15) are tabulated in log to base 10 values (in units of s^{-1}). The EC rates increases with increasing temperature and density (Eq. 9). The probability of occupation of parent excited states increases with increasing stellar temperature and hence contribute effectively to the total rates at high temperatures. It is to be noted that the Fermi energy of electrons increases with increasing stellar densities. This leads to substantial increment of EC rates at high density. However at high densities the rate of change of EC decreases with temperature. The complete set of these rates for all isotopes of chromium can be requested from the authors on demand.

The calculated EC rates on selected chromium isotopes ^{50}Cr, ^{51}Cr, ^{53}Cr, ^{56}Cr and ^{57}Cr of astrophysical importance are shown in Fig. 3. Isotopes of chromium, namely ^{51,53,56,57}Cr, were included in the Aufderheide's list of key nuclei for electron capture rates [5]. In addition, ^{50}Cr, ^{51}Cr, and ^{53}Cr were considered amongst the most important nuclei for modeling of presupernova evolution of massive stars that decrease Y_e of stellar matter (for detail see [6]). Graphs in Fig. 3 illustrate that the EC rates remain, more or less, constant in low density regions. In these regions the beta-decay compete well with capture rates before core collapse. As the stellar core stiffens to high values ($10^8 gcm^{-3} - 10^{11} gcm^{-3}$), the electron Fermi energy also increases thereby increasing the EC rates. At later phases of the collapse, β-decay becomes insignificant as an increased electron chemical potential, which grows like $\rho^{1/3}$ during in fall, considerably, decreases the phase space. These high EC rates during the collapse make the stellar composition more neutron-rich. Thus in the final state of the collapse phase the β-decay is relatively trivial due to Pauli-blocking of the electron phase space [35].

Large scale shell model (LSSM) was used to calculate the EC rates on $^{45-58}$Cr [36]. Fuller, Fowler, and Newman (FFN) [3], on the other hand, used their model to calculate EC rates on $^{45-60}$Cr isotopes. The FFN rates had been used in many simulation codes (e.g., KEPLER stellar evolution code) while LSSM rates were employed in recent simulation of presupernova evolution of massive stars in the mass range 11-40 $M_\odot$ [6]. The comparison of our results with the FFN [3] and large scale shell model (LSSM) rates [36] are shown in Figures 4 and 5. In these figures, for each isotope, we depict three panels. In each case the upper panel shows comparison of calculated EC rates at temperature $1 \times 10^9 K$, whereas the middle and lower panels show comparison at temperatures $10 \times 10^9 K$ and $30 \times 10^9 K$, respectively. The selected values of densities are 10^3 gcm^{-3}, 10^7gcm^{-3} and 10^{11}gcm^{-3} (corresponding to low, medium and high densities). Comparison of the capture rates with

previous calculations can be divided into two categories. In first category our rates are enhanced at all temperatures and densities compared to previous calculations by as much as two orders of magnitude. The results are shown in Fig. 4. Unmeasured matrix elements for allowed transitions were assigned an average value of $logft$ =5 in FFN calculation. On the other hand these transitions were calculated in a microscopic fashion using the pn-QRPA theory (and LSSM) and depict a more realistic picture of the events taking place in stellar environment. The total strengths, centroids and widths of our calculated GT distribution can be seen in Table 2. Both EC and positron-decay rates are very sensitive to the position of the GT_+ centroid. The (n,p) experiment on a nuclide (Z, A) demonstrates the position where in (Z-1, A) the GT_+ centroid analogous to the ground state of (Z, A) resides. The electron capture and β^+-decay are exponentially sensitive to the placement of GT_+ resonance whereas the total $B(GT_+)$ affect the astrophysical rates in a more or less linear fashion [37]. The widths of calculated GT distribution provide a measure of how much the individual GT states are dispersed around the centroid value. The total $B(GT_+)$ strength decreases monotonically as the mass number increases. For both even and odd mass nuclei, the GT resonance energy for FFN cluster around 2, 4, and 6 MeV. The LSSM calculated centroid energies are dispersed as the residual interaction fragment the GT strength (see Fig. 6 of [38]). Table 2 clearly shows that the pn-QRPA calculated centroid energies of GT strength are also scattered due to fragmentation of the GT strength. Compared to the LSSM centroids, FFN place the GT resonance energy usually at higher excitation energies for even-even nuclei and often at too low excitation energies for odd-odd nuclei. FFN place the GT resonance energy at around 6 MeV for odd-A nuclei having odd number of neutrons. Compared to the pn-QRPA and LSSM calculated GT centroids, the FFN estimate for these nuclei are too high. The EC rates calculated by the pn-QRPA model are bigger than those calculated by FFN and LSSM due to lower placement of centroids in our model. The pn-QRPA calculated centroid values of $B(GT_+)$ strength distributions for some important nickel isotopes are shown in Table 3. For comparison the centroids calculated by LSSM, FFN and those by Pruet and Fuller [39] are also given. In the last column centroids of measured $B(GT_+)$ strength distributions are shown. Measured data was taken from [40, 41]. The pn-QRPA calculated centroids values are in reasonable agreement with the experimental data, except for ^{62}Ni.

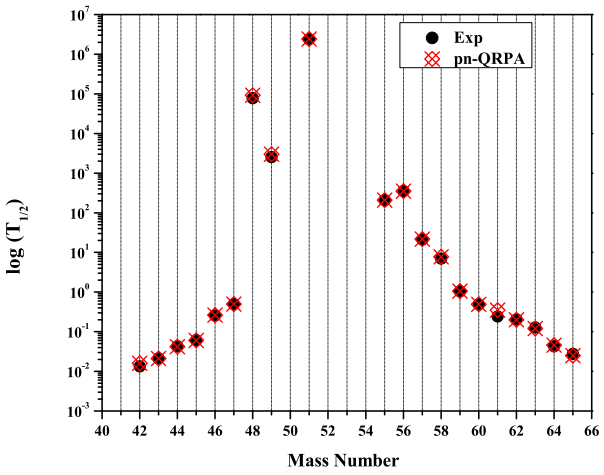

Fig. 1 – Total β-decay half-lives for Cr isotopes calculated from the pn-QRPA model (this work) in comparison with the experimental data [29]. $^{50,52-54}$Cr are stable.

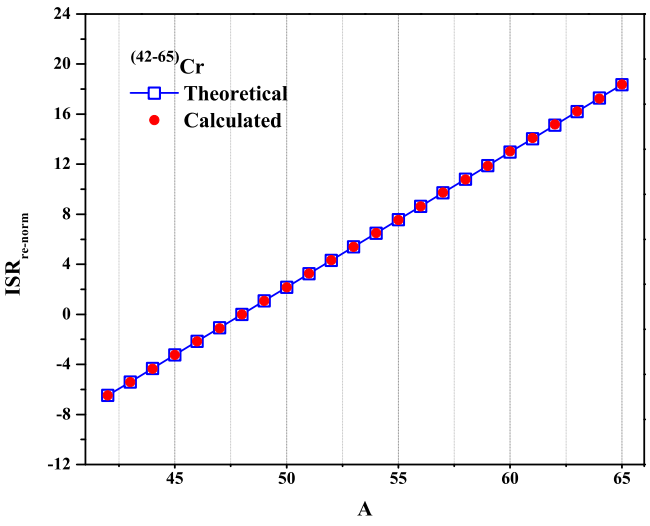

Fig. 2 – Comparison of calculated and theoretical re-normalized Ikeda Sum Rule.

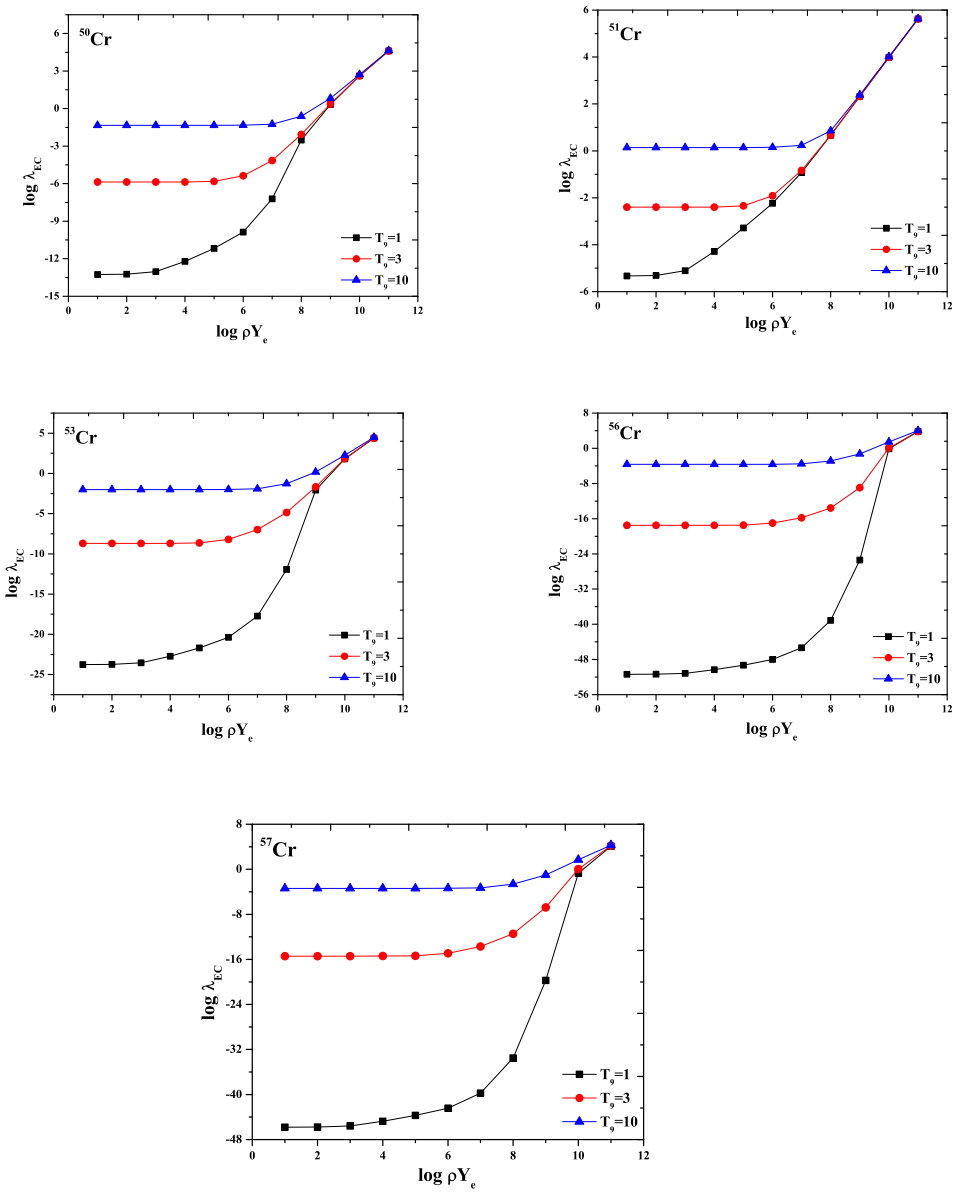

Fig. 3 – Electron capture rates on (^{50,51,53,56,57}Cr) isotopes as function of stellar densities (ρY_e) having units of g/cm^3 at different selected temperatures. Temperatures (T_9) are given in units of 10^9 K and $\log \lambda_{EC}$ represents the log (to base 10) of EC rates in units of s^{-1}.

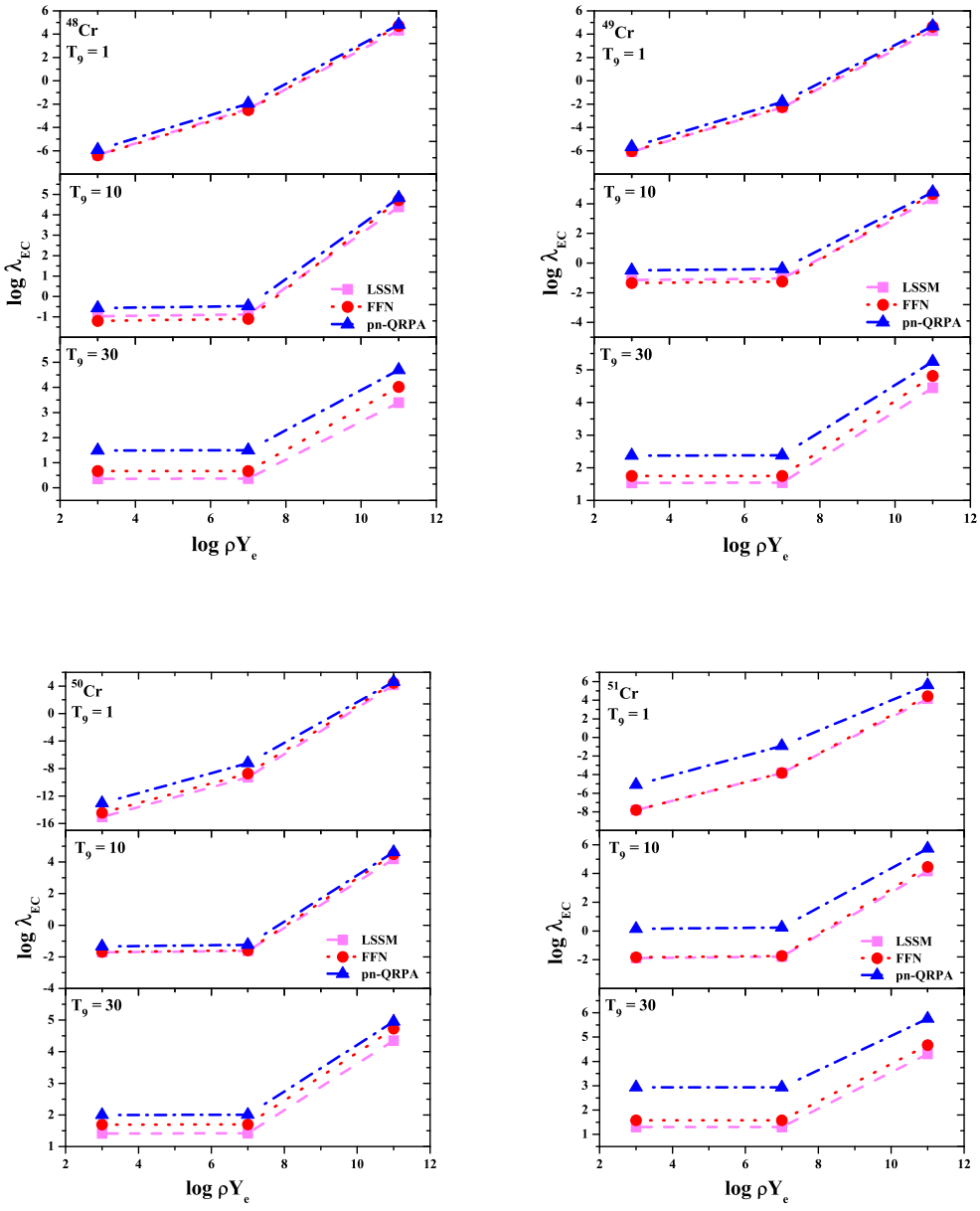

Fig. 4 – Comparison of EC rates of pn-QRPA (this work) with those of FFN [3] and large scale shell model (LSSM) [36] as function of stellar densities (ρY_e) having units of g/cm^3 at different selected temperatures. Temperatures (T_9) are given in units of 10^9 K and $\log \lambda_{EC}$ represents the log (to base 10) of EC rates in units of s^{-1}.

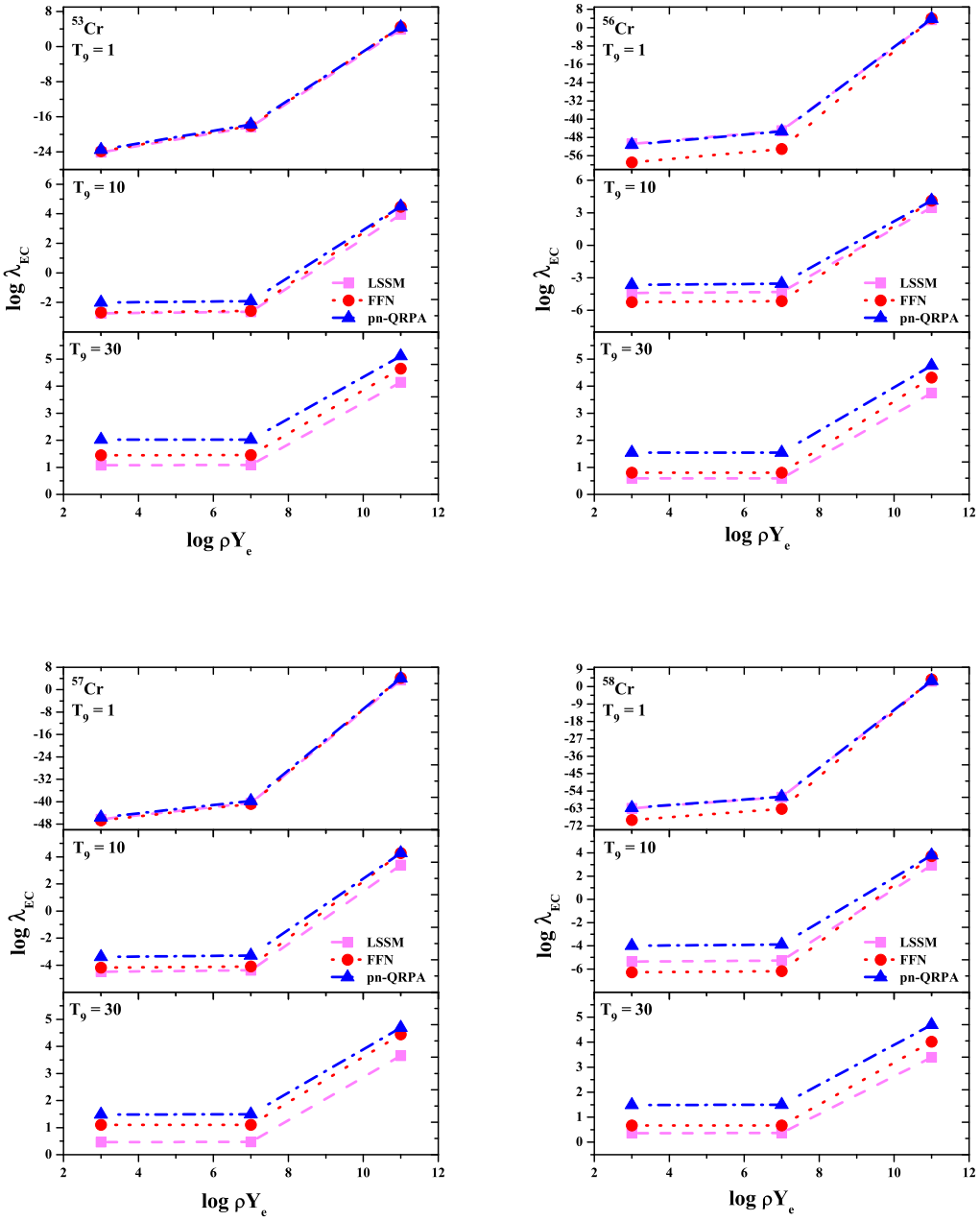

Fig. 5 – Same as Fig. 4, but for $^{53,56-58}$Cr isotopes.

Table 1

Calculated EC rates in stellar region on chromium ($^{42-65}$Cr) isotopes at various densities and temperatures. The first column shows the stellar densities (ρY_e) (in units of g/cm^3), where ρ is the baryon density and Y_e is the ratio of the electron number to the baryon number. T_9 are given in units of 10^9 K. The calculated EC rates are tabulated in log to base 10 scale and given in units of s^{-1}.

$\log \rho Y_e$	T_9	^{42}Cr	^{43}Cr	^{44}Cr	^{45}Cr	^{46}Cr	^{47}Cr	^{48}Cr	^{49}Cr	^{50}Cr	^{51}Cr	^{52}Cr	^{53}Cr
3	1	-3.239	-3.396	-3.428	-3.383	-3.935	-4.294	-5.917	-5.674	-13.029	-5.104	-26.535	-23.539
3	3	-0.941	-1.057	-1.119	-1.090	-1.609	-1.848	-3.314	-3.062	-5.872	-2.401	-10.061	-8.695
3	10	0.990	0.946	0.860	0.848	0.489	0.252	-0.571	-0.501	-1.341	0.141	-2.246	-2.010
3	30	3.054	3.343	3.158	3.215	2.803	2.466	2.274	2.373	1.999	2.934	1.802	2.021
7	1	0.463	0.305	0.283	0.327	-0.209	-0.576	-1.954	-1.818	-7.209	-0.924	-20.724	-17.736
7	3	0.474	0.358	0.301	0.331	-0.180	-0.425	-1.789	-1.572	-4.159	-0.833	-8.358	-6.984
7	10	1.082	1.038	0.953	0.940	0.582	0.344	-0.475	-0.405	-1.244	0.238	-2.148	-1.911
7	30	3.058	3.347	3.161	2.806	3.218	2.470	2.278	2.377	2.003	2.938	1.806	2.024
11	1	5.360	5.263	5.338	5.375	5.098	4.860	4.811	4.688	4.611	5.625	4.510	4.394
11	3	5.361	5.273	5.338	5.389	5.099	4.910	4.812	4.726	4.611	5.627	4.511	4.396
11	10	5.385	5.338	5.364	5.395	5.153	5.081	4.832	4.774	4.631	5.630	4.539	4.498
11	30	5.633	5.905	5.775	5.478	5.862	5.202	5.120	5.254	4.949	5.762	4.889	5.112
$\log \rho Y_e$	T_9	^{54}Cr	^{55}Cr	^{56}Cr	^{57}Cr	^{58}Cr	^{59}Cr	^{60}Cr	^{61}Cr	^{62}Cr	^{63}Cr	^{64}Cr	^{65}Cr
3	1	-40.534	-34.933	-51.155	-45.571	-62.707	-55.426	-73.862	-68.342	-86.371	-75.944	-95.139	-81.490
3	3	-13.788	-11.869	-17.515	-15.417	-20.408	-18.451	-23.950	-23.113	-28.681	-26.338	-30.957	-27.670
3	10	-2.952	-2.403	-3.647	-3.386	-3.992	-3.894	-4.995	-5.746	-7.168	-7.703	-7.066	-7.735
3	30	1.634	1.895	1.540	1.485	1.491	1.392	1.263	0.449	-0.212	-0.712	0.593	-0.523
7	1	-34.714	-29.113	-45.335	-39.751	-56.887	-49.606	-68.042	-62.522	-80.552	-70.124	-89.319	-75.670
7	3	-12.073	-10.153	-15.799	-13.702	-18.693	-16.736	-22.235	-21.398	-26.965	-24.622	-29.241	-25.955
7	10	-2.854	-2.304	-3.548	-3.288	-3.893	-3.795	-4.897	-5.647	-7.069	-7.604	-6.967	-7.636
7	30	1.638	1.898	1.543	1.489	1.495	1.395	1.266	0.453	-0.209	-0.708	0.596	-0.520
11	1	4.423	4.394	3.829	4.080	2.985	3.449	2.578	3.000	2.403	2.210	1.766	2.516
11	3	4.424	4.483	3.831	4.180	2.988	3.396	2.583	3.297	2.413	2.313	1.787	2.512
11	10	4.458	4.667	4.137	4.283	3.791	3.715	3.161	3.692	3.013	2.843	3.054	2.655
11	30	4.819	5.062	4.753	4.691	4.696	4.619	4.585	3.982	3.422	3.009	4.212	3.215

In the other category at lower stellar temperatures our rates are in reasonable agreement with LSSM results. However in case of ^{56,58}Cr isotopes at low density and temperature region, our rates and LSSM rates are enhanced by around seven orders of magnitude as compared to FFN EC rates. At high density and low temperature region the mutual comparison between all calculations is decent. Figure 5 shows the mutual comparison of EC rates for this category. At high temperatures and density region the situation is more interested if we compare the results of LSSM and FFN. At high temperature and density region, the LSSM rates are too small as compared to FFN and pn-QRPA rates. The Lanczos-based approach used by LSSM and pointed by [39] provides the reason for this discrepancy. The calculated LSSM decay rates is a function of the number of Lanczos iterations essential for convergence and this behavior of partition functions can affect their estimates of high temperature weak rates. Accordingly at high temperatures the LSSM rates tend to be too low. The pn-QRPA calculation do not suffer from this convergence problem as it is not Lanczos-based. At high temperatures, where the occupation probability of excited states is larger, our EC rates for all isotopes are enhanced by an order of magnitude as compared to LSSM rates. There are several other reasons for the enhancement of our rates. The pn-QRPA model provides adequate model space which effectively handle all the excited states in parent as well as in daughter nuclei. We also do not

Table 2

The pn-QRPA calculated total B(GT) strengths, centroids and widths of Cr isotopes in electron capture direction.

Nuclei	$\sum$ B(GT$_+$)	$\bar{E}_+$ (MeV)	Width$_+$ (MeV)
^{42}Cr	7.08	6.80	3.25
^{43}Cr	5.95	9.74	3.10
^{44}Cr	5.33	7.96	5.55
^{45}Cr	4.24	7.95	3.09
^{46}Cr	4.31	4.76	3.31
^{47}Cr	3.24	8.81	3.26
^{48}Cr	3.33	4.19	2.56
^{49}Cr	2.23	7.90	2.04
^{50}Cr	2.49	4.03	2.41
^{51}Cr	1.87	7.96	2.41
^{52}Cr	2.21	3.23	2.01
^{53}Cr	0.51	6.21	2.71
^{54}Cr	1.95	2.11	3.68
^{55}Cr	0.39	4.06	3.47
^{56}Cr	1.31	1.77	2.14
^{57}Cr	0.25	5.21	2.84
^{58}Cr	0.82	1.57	2.49
^{59}Cr	0.24	1.26	2.24
^{60}Cr	0.39	3.03	4.99
^{61}Cr	0.21	3.79	3.41
^{62}Cr	0.23	3.22	5.51
^{63}Cr	0.17	1.83	2.69
^{64}Cr	0.16	2.63	5.06
^{65}Cr	0.12	2.87	3.31

consider the Brink's hypothesis in our calculations to approximate the contribution from parent excited levels. This approximation was used both by FFN and LSSM. Brink's hypothesis states that GT strength distribution on excited states is *identical* to that from ground state, shifted *only* by the excitation energy of the state. We carried out a state-by-state calculation of these capture rates from parent to daughter states in a microscopic way and added them at the end to obtain the total EC rates (Eq. 15). It is further to be noted that both LSSM and pn-QRPA model perform a microscopic calculation of all energy eigenvalues and GT matrix elements for ground state of parent nucleus. Accordingly, whenever ground state rates command the total rate, the

Table 3

The pn-QRPA calculated centroids for nickel isotopes compared with other theoretical calculations and measurements. Centroid energies are given in units of MeV. For references see text.

Nucleus	$\bar{E}_+$ [pn-QRPA]	$\bar{E}_+$[PF]	$\bar{E}_+$[FFN]	$\bar{E}_+$[LSSM]	$\bar{E}_+$[exp]
^{58}Ni	3.57	3.65	3.76	3.75	3.60±0.20
^{60}Ni	3.09	2.70	2.00	2.88	2.40±0.30
^{61}Ni	4.93	4.70	-	4.70	-
^{62}Ni	2.13	1.80	2.00	1.78	1.30±0.30
^{64}Ni	0.80	1.80	2.00	0.50	0.80±0.30

Table 4

Ratio of calculated electron capture (EC) rates to β^+-decay for different selected densities and temperatures. The second column shows the stellar densities (ρY_e) (in units of g/cm^3). T_9 are given in units of 10^9 K.

Nucleus	ρY_e	$R(EC/\beta^+)$			
		T_9=01	T_9=05	T_9=10	T_9=30
^{42}Cr	10^7	6.6E-02	7.5E-02	2.2E-01	4.4E+00
	10^9	1.0E+01	1.1E+01	1.0E+01	8.6E+00
	10^{11}	5.2E+03	5.2E+03	4.4E+03	1.5E+03
^{43}Cr	10^7	4.2E-02	4.0E-02	8.9E-02	2.5E+00
	10^9	6.8E+00	5.7E+00	3.9E+00	4.8E+00
	10^{11}	3.8E+03	2.9E+03	1.8E+03	8.4E+02
^{44}Cr	10^7	1.2E-01	1.4E-01	4.3E-01	1.2E+01
	10^9	2.1E+01	2.2E+01	2.1E+01	2.3E+01
	10^{11}	1.3E+04	1.3E+04	1.1E+04	4.4E+03
^{45}Cr	10^7	1.8E-01	2.1E-01	7.3E-01	2.3E+01
	10^9	3.4E+01	3.4E+01	3.5E+01	4.3E+01
	10^{11}	2.2E+04	2.1E+04	2.0E+04	8.7E+03
^{46}Cr	10^7	2.3E-01	2.9E-01	9.1E-01	4.4E+01
	10^9	5.4E+01	5.6E+01	4.7E+01	8.2E+01
	10^{11}	4.7E+04	4.7E+04	3.3E+04	1.7E+04
^{47}Cr	10^7	2.5E-01	3.0E-01	1.2E+00	9.1E+01
	10^9	5.4E+01	5.3E+01	5.9E+01	1.7E+02
	10^{11}	6.9E+04	5.3E+04	5.0E+04	3.9E+04
^{48}Cr	10^7	1.5E+03	4.6E+02	2.0E+01	3.5E+02
	10^9	2.1E+06	2.8E+05	1.7E+03	6.5E+02
	10^{11}	8.6E+09	1.0E+09	3.9E+06	1.9E+05
^{49}Cr	10^7	2.9E+01	3.3E+01	6.1E+01	2.0E+03
	10^9	2.6E+04	1.4E+04	4.2E+03	3.6E+03
	10^{11}	9.2E+07	3.8E+07	8.5E+06	1.1E+06
^{50}Cr	10^7	2.9E+14	8.8E+02	7.9E+01	1.8E+03
	10^9	9.6E+21	2.8E+06	8.3E+03	3.3E+03
	10^{11}	1.9E+26	4.1E+10	5.4E+07	1.2E+06
^{51}Cr	10^7	6.5E+07	9.0E+04	6.7E+03	2.3E+04
	10^9	1.1E+11	5.0E+07	4.9E+05	4.2E+04
	10^{11}	2.3E+14	9.4E+10	1.5E+09	1.2E+07
^{52}Cr	10^7	5.2E+11	5.1E+03	6.5E+02	8.8E+03
	10^9	2.2E+30	7.7E+07	8.1E+04	1.6E+04
	10^{11}	8.9E+36	4.2E+13	2.9E+09	8.1E+06
^{53}Cr	10^7	1.2E+23	1.2E+06	3.7E+04	2.1E+06
	10^9	5.2E+38	4.6E+09	4.1E+06	3.6E+06
	10^{11}	1.6E+45	1.0E+15	8.4E+10	1.7E+09
^{54}Cr	10^7	9.5E+14	1.2E+06	3.3E+05	3.2E+07
	10^9	1.0E+35	2.7E+10	4.7E+07	5.3E+07
	10^{11}	1.3E+54	5.2E+17	5.5E+12	2.9E+10

two calculations are found to be in excellent agreement. For cases where excited state partial rates influence the total rate, differences are seen between the two calculations.

One important question could be to know how the electron capture rates compete with the positron decay (PD) rates for these isotopes of chromium during presupernova evolution of massive stars. Table 4 displays the ratio of calculated EC to PD rates at selected temperatures (1, 5, 10 and 30)$\times 10^9 K$ and densities (10^7, 10^9 and $10^{11} gcm^{-3}$). It is observed that in $^{42-47}$Cr nuclides at stellar temperatures (1, 5, and 10)$\times 10^9 K$ and density 10^7 gcm^{-3}, β^+-decay rates are greater than the EC rates by 1-2 orders of magnitude and must be taken into account in simulation codes. At high densities ($10^9 - 10^{11}$) g/cm^3 the EC rates are bigger than the competing β^+ rates by 1-4 orders of magnitude. As mentioned before the electron Fermi energy increases at high densities which in turn lead to significant enhancement in calculated electron capture rates. As $N \geq Z$, it is clear from Table 4 that the EC rates exceed the competing β^+ rates both in low and high temperature and density region. The PD values decrease as the neutron number (*N*) increases. As $N \geq 31$, calculated PD rates become less than 10^{-100} and are not shown in Table 4. For all these isotopes the PD rates can safely be neglected in comparison with the EC rates.

4. CONCLUSIONS

Chromium isotopes are advocated to play a vital role among the iron-regime nuclide controlling the dynamics of core-collapse of massive stars. The EC rates on Cr isotopes may be used as a nuclear physics input parameter for core-collapse simulation codes. Here we present the calculation of stellar EC rates on twenty-four isotopes of chromium. We considered a total of 100 parent and daughter excited states (covered energy range was in excess of 10 MeV) for the microscopic calculation of these rates. Our model calculation reproduced well the measured β-decay half-life values and also fulfilled the Ikeda Sum Rule. Later we performed calculation of stellar electron capture and positron-decay rates of chromium isotopes. We compared our results with the previous calculations of FFN and LSSM. Our calculated EC rates are enhanced in the presupernova era as compared to previous calculations and this is an interesting finding. From astral viewpoint these enhanced EC rates may have substantial impact on the late stage evolution of massive stars and the shock waves energetics. Results of simulations illustrate that EC rates have a solid effect on the core collapse trajectory and on the properties of the core at bounce. We urge collapse simulators to test run our calculated EC rates in their codes to search for possible interesting outcomes. β^+ decay rates are only important for $N \leq Z$ chromium isotopes up to stellar density of $10^7 gcm^{-3}$. For remaining chromium isotopes and

higher temperature-density regions, the β^+ decay rates can safely be neglected when compared with the corresponding EC rates.

Acknowledgements. J.-U. Nabi would like to acknowledge the support of the Higher Education Commission Pakistan through the HEC Project No. 20-3099.

REFERENCES

1. H. A. Bethe, G. E. Brown, J. Applegate and J. M. Lattimer, Nucl. Phys. A **324**, 487 (1979).
2. S. Chandrasekhar, *An Introduction to the Study of Stellar Structure*, Univ. of Chicago Press (1939).
3. G. M. Fuller, W. A. Fowler and M. J. Newman, Astrophys. J. Suppl. Ser. **42**, 447 (1980); **48**, 279 (1982); Astrophys. J. **252**, 715 (1982).
4. S. Cakmak, J.-U. Nabi, T. Babacan and I. Maras, Adv. Space Res. **55**, 440-453 (2015).
5. M. B. Aufderheide, I. Fushiki, S. E. Woosley and D. H. Hartmann, Astrophys. J. Suppl. Ser. **91**, 389 (1994).
6. A. Heger, S. E. Woosley, G. Martínez-Pinedo and K. Langanke, Astrophys. J. **560**, 307 (2001).
7. J. Zioni, A. A. Jaffe, E. FriedMan, N. Haik, R. Schectman and D. Nir, Nucl. Phys. A **181**, 465-476 (1972).
8. Y. Fujita, B. Rubio and W. Gelletly, Prog. Part. Nucl. Phys. **66**, 549-606 (2011).
9. T. Adachi et al., Nucl. Phys. A **788**, 70c-75c (2007).
10. J.-U. Nabi and C. W., Johnson, J. Phys. G **40**, 065202 (2013).
11. J.-U. Nabi and M. Sajjad, Phys. Rev. C **76**, 055803 (2007).
12. J.-U. Nabi, M. Sajjad and M.-U. Rahman, Acta Phys. Pol. B **38**, 3203 (2007).
13. J. A. Halbleib and R. A. Sorensen, Nucl. Phys. A **98**, 542 (1967).
14. J. Krumlinde and P. Möller, Nucl. Phys. A **417**, 419 (1984).
15. K. Muto, E. Bender and H. V. Klapdor, Z. Phys. A **333**, 125 (1989).
16. A. Staudt, E. Bender, K. Muto and H. V. Klapdor, Z. Phys. A **334**, 47 (1989).
17. M. Hirsch, A. Staudt, K. Muto and H. V. Klapdor-Kleingrothaus, At. Data Nucl. Data Tables **53**, 165 (1993).
18. K. Muto, E. Bender, T. Oda and H. V. Klapdor, Z. Phys. A **341**, 407 (1992).
19. J.-U. Nabi and H. V. Klapdor-Kleingrothaus, At. Data Nucl. Data Tables **71**, 149 (1999).
20. J.-U. Nabi and H. V. Klapdor-Kleingrothaus, At. Data Nucl. Data Tables **88**, 237 (2004).
21. J.-U. Nabi and H. V. Klapdor-Kleingrothaus, Eur. Phys. J. A **5**, 337 (1999).
22. S. G. Nilsson, Mat. Fys. Medd. Dan. Vid. Selsk **29**, 1-68 (1955).
23. K. Ikeda, S. Fujii and J. I. Fujita, Phys. Lett. **3**, 271 (1963).
24. H. Homma, E. Bender, M. Hirsch, K. Muto, H. V. Klapdor-Kleingrothaus and T. Oda, Phys. Rev. C **54**, 2972 (1996).
25. I. Ragnarsson and R. K. Sheline, Phys. Scr. **29**, 385 (1984).
26. M. Hirsch, A. Staudt, K. Muto and H. V. KlapdorKleingrothaus, Nucl. Phys. A **535**, 62 (1991).
27. S. Raman, C. H. Malarkey, W. T. Milner, C. W. Nestor and P. H. Jr. Stelson, At. Data Nucl. Data Tables **36**, 1 (1987).
28. P. Möller and J. R. Nix, At. Data Nucl. Data Tables **26**, 165 (1981).
29. G. Audi et al., Chinese Physics C **36**, 1157 (2012).
30. N. B. Gove and M. J. Martin, Atomic Data and Nuclear Data Tables **10**, 205 (1971).
31. K. Grotz and H. V. Klapdor, *The Weak Interaction in Nuclear, Particle and Astrophysics*, Adam

Hilger, (IOP Publishing, Bristol, Philadelphia, New York) (1990).
32. M. C. Vetterli, O. Häusser, R. Abegg, W. P. Alford, A. Celler, D. Frekers, R. Helmer, R. Henderson, K. H. Hicks, K. P. Jackson, R. G. Jeppesen, C. A. Miller, K. Raywood and S. Yen, Phy. Rev. C **40**, 559 (1989).
33. C. Gaarde, Nucl. Phys. A **396**, 127c (1983).
34. T. Rönnqvist, H. Condé, N. Olsson, E. Ramström, R. Zorro, J. Blomgren, A. Håkansson, A. Ringbom, G. Tibell, O. Jonsson, L. Nilsson, P.-U. Renberg, S. Y. van der Werf, W. Unkelbach and F. P. Brady, Nucl. Phys. A **563**, 225 (1993).
35. J.-U. Nabi and M.-U. Rahman, Phys. Lett. B **612**, 190 (2005).
36. K. Langanke and G. Martinez-Pinedo, At. Data and Nucl.Data Tables **79**, 1 (2001).
37. M. B. Aufderheide et al., Phys. Rev. C **53**, 3139-3142 (1996).
38. K. Langanke and G. Martinez-Pinedo, Nucl. Phys. A **673**, 481 (2000).
39. J. Pruet and G. M. Fuller, Astrophys. J. Suppl. Ser. **149** 189-203 (2003).
40. A. L. Williams et al., Phys. Rev. C **51**, 1144 (1995).
41. S. El-Kateb et al., Phys. Rev. C **49**, 3128 (1994).